Chapter 8

Aeroelastic Stability of Turboprop Aircraft: Whirl Flutter

Jiří Čečrdle

Additional information is available at the end of the chapter

http://dx.doi.org/10.5772/intechopen.70171

Abstract

This chapter is focused on a specific type of dynamic aeroelastic stability phenomenon—whirl flutter. Whirl flutter is caused by the effect of rotating parts of a turboprop power plant (propeller and, gas turbine engine rotor). The chapter presents fundamental facts regarding the whirl flutter phenomenon, including a historical overview and information regarding the occurrence of whirl flutter in aerospace practice. After that, the physical principles of whirl flutter are explained using a simple mechanical system with two degrees of freedom. Next, an analytical solution to determine the aerodynamic forces caused by the gyroscopic motion on each of the propeller blades is provided and the influences of the main structural parameters on the whirl flutter stability are discussed. The second, practical part is focused on the experimental research of the whirl flutter phenomenon and on the certification-related issues. The methodology of certification according to the FAR/CS 23 regulation standard is demonstrated on the example of a twin wing mounted tractor engine commuter aircraft.

Keywords: aeroelasticity, flutter, whirl flutter, quasi-steady theory, gyroscopic system

1. Introduction

Whirl flutter instability is a specific type of aeroelastic flutter instability that may appear on turboprop aircraft. It accounts for the dynamic and aerodynamic effects of rotating parts, such as a gas turbine engine rotor or a propeller. The rotating mass increases the number of degrees of freedom and generates additional forces and moments. Rotating propellers also cause an aerodynamic interference effect between a propeller and the structure of a nacelle and a wing. Whirl flutter instability is driven by motion-induced unsteady aerodynamic propeller forces and moments acting on the propeller plane. It may cause unstable vibration, which can lead to failure of an engine installation or an entire wing.

The propeller whirl flutter phenomenon was analytically discovered by Taylor and Browne [1]. The next pioneering work was performed by Ribner, who set the basic formulae for the aerodynamic derivatives of propeller forces and moments due to the motion and velocities in pitch and yaw in 1945 [2, 3]. After the accidents of two Lockheed L-188 C Electra II airliners in 1959 and 1960 [4], the importance of the whirl flutter phenomenon in practical applications was recognised.

This chapter is focused on turboprop aircraft whirl flutter; however, it may also occur in tilt-rotor aircraft. The whirl flutter phenomenon relates the mutual interactions of the rotating propeller with the aircraft deformations and the aerodynamic forces emerging during forward flight.

2. Physical principle and analytical solution

The principle of the whirl flutter phenomenon is outlined on a simple mechanical system with two degrees of freedom [5]. The propeller and hub are considered to be rigid. A flexible engine mounting is substituted with a system of two rotational springs (of stiffnesses K_Ψ and K_Θ), as illustrated in **Figure 1**.

Such a system has two independent mode shapes of yaw and pitch, with respective angular frequencies of ω_Ψ and ω_Θ, as shown in **Figure 2**.

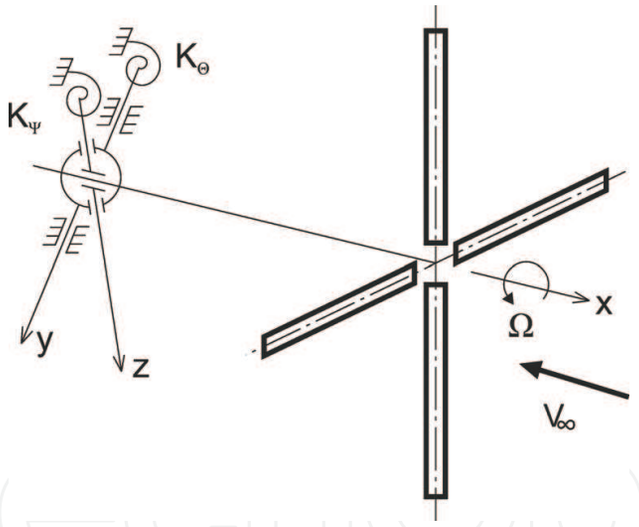

Figure 1. Two-degree-of-freedom gyroscopic system with a propeller.

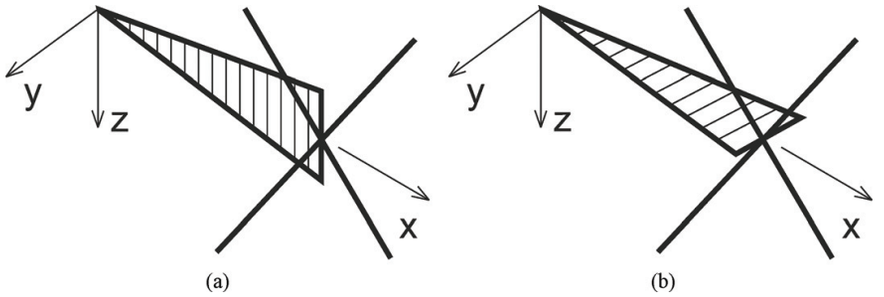

Figure 2. Independent engine pitch (a) and yaw (b) mode shapes.

http://dx.doi.org/10.5772/intechopen.70171

Considering the propeller rotation with angular velocity Ω, the primary system motion changes to the characteristic gyroscopic motion. The gyroscopic effect causes two independent mode shapes to merge into whirl motion as shown in **Figure 3**. The axis of a propeller makes an elliptical movement. The orientation of the propeller axis movement is backward relative to the propeller rotation for the lower-frequency mode (backward whirl mode) and is forward relative to the propeller rotation for the higher-frequency mode (forward whirl mode). The trajectory of this elliptical movement depends on both angular frequencies ω_Ψ and ω_Θ. Because the yaw and pitch motions have a 90° phase shift, the mode shapes in the presence of gyroscopic effects are complex.

The described gyroscopic motion causes the angles of attack of the propeller blades to change, which consequently leads to unsteady aerodynamic forces. These forces may, under specific conditions, induce whirl flutter instability. The most important terms regarding whirl flutter are yaw moment due to pitch $M_Z(\Theta)$ and, similarly pitch moment due to yaw $M_Y(\Psi)$. These moments are to be balanced by aerodynamic or structural damping terms. The state of neutral stability with no damping of the system represents the flutter state. The corresponding airflow ($V_\infty = V_{FL}$) is called the critical flutter speed. In terms of flutter, the stable and unstable states of the gyroscopic system are applicable. Both states for the backward mode are explained in **Figure 4**. As long as the air velocity is lower than a critical value ($V_\infty < V_{FL}$), the system is stable

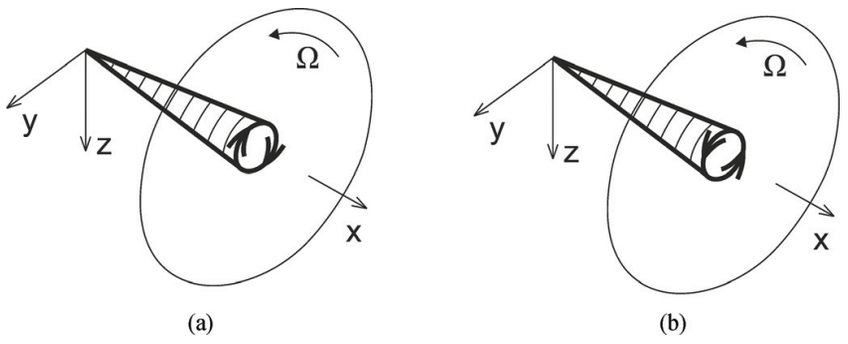

Figure 3. Backward (a) and forward (b) whirl modes.

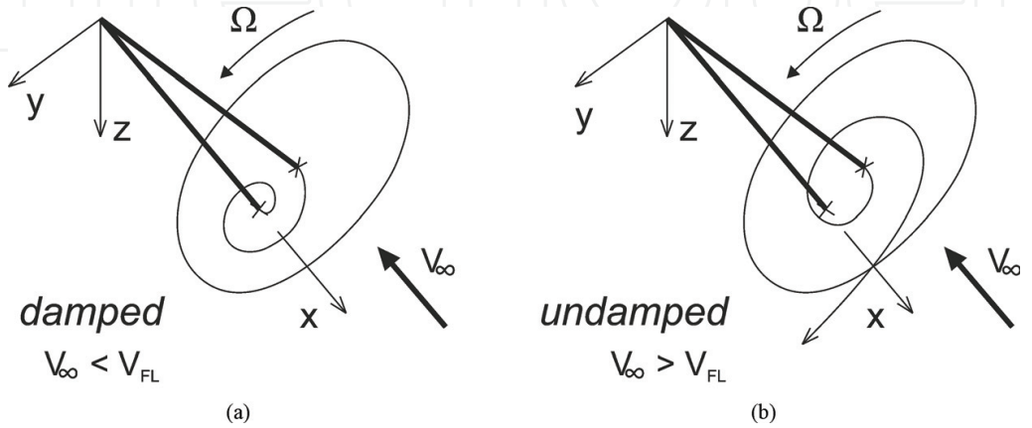

Figure 4. Stable (a) and unstable (b) states of gyroscopic vibrations for the backward mode.

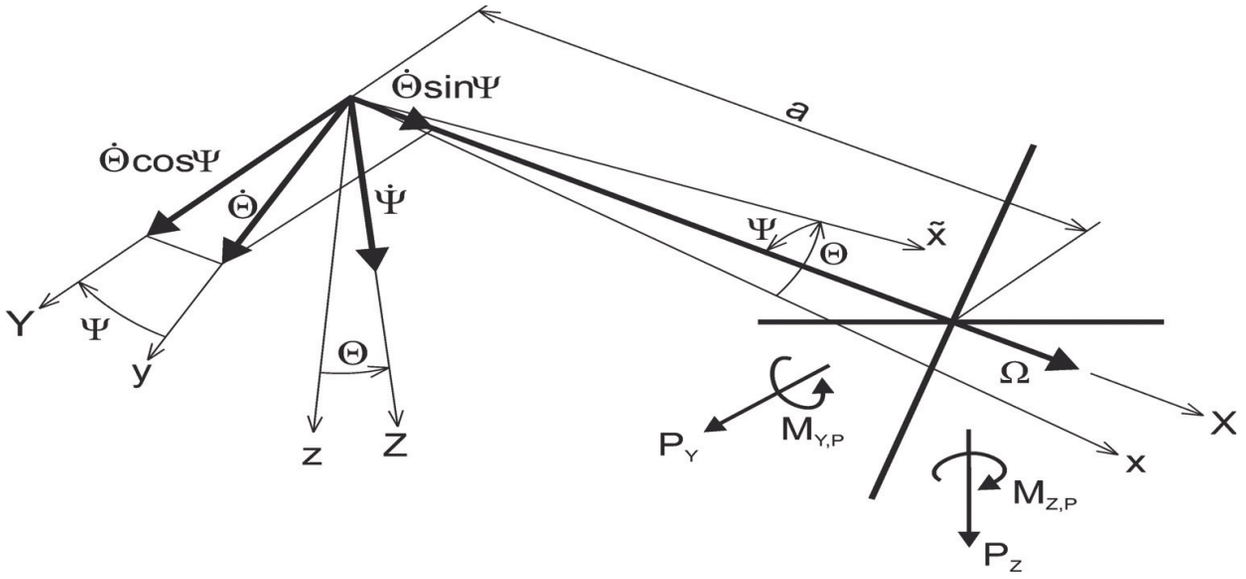

Figure 5. Kinematical scheme of the gyroscopic system.

and the gyroscopic motion is damped. When the airspeed exceeds the critical value ($V_\infty > V_{FL}$), the system becomes unstable and the gyroscopic motion is divergent.

The main problem in obtaining the analytical solution is to determine the aerodynamic force caused by the gyroscopic motion on each of the propeller blades. The presented equations of motion were set up for the system described in **Figure 1** by means of Lagrange's approach. The kinematical scheme, including gyroscopic effects, is shown in **Figure 5**.

Three angles (φ, Θ, Ψ) are selected as the independent generalised coordinates. The propeller is assumed to be cyclically symmetric with respect to both mass and aerodynamics (i.e., a propeller with a minimum of three blades). The angular velocity is considered to be constant ($\varphi = \Omega t$). Nonuniform mass moments of inertia of the engine with respect to the yaw and pitch axes ($J_Y \neq J_Z$) are also considered. We will use a coordinate system X, Y, Z linked to the system. Then, kinetic energy is:

$$E_K = \frac{1}{2} J_X \omega_X^2 + \frac{1}{2} \left(J_Y \omega_Y^2 + J_Z \omega_Z^2 \right) \tag{1}$$

The angular velocities will be

$$\begin{aligned} \omega_X &= \Omega + \dot{\Theta} \sin\Psi \approx \Omega + \dot{\Theta}\Psi \\ \omega_Y &= \dot{\Theta} \cos\Psi \approx \dot{\Theta} \\ \omega_Z &= \dot{\Psi} \end{aligned} \tag{2}$$

Considering that $\dot{\Theta}^2 \dot{\Psi}^2 << \Omega^2$, the equation for the kinetic energy becomes

$$E_K = \frac{1}{2} J_X \Omega^2 + J_X \Omega \Psi \dot{\Theta} + \frac{1}{2} (J_Y \dot{\Theta}^2 + J_Z \dot{\Psi}^2) \tag{3}$$

The first part of Eq. (3) is independent of both Θ and Ψ; thus, it does not appear in Lagrange's equation. Then, the potential energy becomes

$$E_P = \frac{1}{2} K_\Theta \Theta^2 + \frac{1}{2} K_\Psi \Psi^2 \tag{4}$$

To describe the damping, we assume the structural damping commonly used in the flutter analyses, with the damping force proportional to the amplitude of the displacement:

$$D = \frac{1}{2} \frac{K_\Theta \gamma_\Theta}{\omega} \dot{\Theta}^2 + \frac{1}{2} \frac{K_\Psi \gamma_\Psi}{\omega} \dot{\Psi}^2 \tag{5}$$

Then, we obtain from Lagrange's equations and Eqs. (3)–(5) a system of two mutually influencing differential equations:

$$\begin{aligned} J_Y \ddot{\Theta} + \frac{K_\Theta \gamma_\Theta}{\omega} \dot{\Theta} + J_X \Omega \dot{\Psi} + K_\Theta \Theta &= Q_\Theta \\ J_Z \ddot{\Psi} + \frac{K_\Psi \gamma_\Psi}{\omega} \dot{\Psi} - J_X \Omega \dot{\Theta} + K_\Psi \Psi &= Q_\Psi \end{aligned} \tag{6}$$

Generalized propeller forces and moments (see **Figure 5**) can be expressed as

$$\begin{aligned} Q_\Theta &= M_{Y,P} - aP_Z \\ Q_\Psi &= M_{Z,P} + aP_Y \end{aligned} \tag{7}$$

The index P means that the moment around the specific axis is at the plane of the propeller rotation. Employing the quasi-steady theory, the effective angles become

$$\begin{aligned} \Theta^* &= \Theta - \frac{\dot{Z}}{V_\infty} = \Theta - \frac{a\dot{\Theta}}{V_\infty} \\ \Psi^* &= \Psi - \frac{\dot{Y}}{V_\infty} = \Psi - \frac{a\dot{\Psi}}{V_\infty} \end{aligned} \tag{8}$$

Neglecting the aerodynamic inertia terms ($\dot{\Theta}^* \approx \dot{\Theta}$, $\dot{\Psi}^* \approx \dot{\Psi}$), we obtain the equations for the propeller's dimensionless forces and moments as follows:

$$\begin{aligned} P_Y &= q_\infty F_p \left(c_{y\Psi} \Psi^* + c_{y\Theta} \Theta^* + c_{yq} \frac{\dot{\Theta}^* R}{V_\infty} \right) \\ P_Z &= q_\infty F_p \left(c_{z\Theta} \Theta^* + c_{z\Psi} \Psi^* + c_{zr} \frac{\dot{\Psi}^* R}{V_\infty} \right) \\ M_{Y,P} &= q_\infty F_P D_P \left(c_{m\Psi} \Psi^* + c_{mq} \frac{\dot{\Theta}^* R}{V_\infty} \right) \\ M_{Z,P} &= q_\infty F_P D_P \left(c_{n\Theta} \Theta^* + c_{nr} \frac{\dot{\Psi}^* R}{V_\infty} \right) \end{aligned} \tag{9}$$

where F_P is the propeller disc area and D_P is the propeller diameter.

The aerodynamic derivatives representing the derivatives of the two aerodynamic forces and two aerodynamic moments with respect to the pitch and yaw angles and to the pitch and yaw angular velocities are then defined as follows:

$$\begin{aligned}
c_{y\Theta} &= \frac{\partial c_y}{\partial \Theta^*} \quad c_{y\Psi} = \frac{\partial c_y}{\partial \Psi^*} \quad c_{yq} = \frac{\partial c_y}{\partial\left(\frac{\dot{\Theta} R}{V_\infty}\right)} \quad c_{yr} = \frac{\partial c_y}{\partial\left(\frac{\dot{\Psi} R}{V_\infty}\right)} \\
c_{z\Theta} &= \frac{\partial c_z}{\partial \Theta^*} \quad c_{z\Psi} = \frac{\partial c_z}{\partial \Psi^*} \quad c_{zq} = \frac{\partial c_z}{\partial\left(\frac{\dot{\Theta} R}{V_\infty}\right)} \quad c_{zr} = \frac{\partial c_z}{\partial\left(\frac{\dot{\Psi} R}{V_\infty}\right)} \\
c_{m\Theta} &= \frac{\partial c_m}{\partial \Theta^*} \quad c_{m\Psi} = \frac{\partial c_m}{\partial \Psi^*} \quad c_{mq} = \frac{\partial c_m}{\partial\left(\frac{\dot{\Theta} R}{V_\infty}\right)} \quad c_{mr} = \frac{\partial c_m}{\partial\left(\frac{\dot{\Psi} R}{V_\infty}\right)} \\
c_{n\Theta} &= \frac{\partial c_n}{\partial \Theta^*} \quad c_{n\Psi} = \frac{\partial c_n}{\partial \Psi^*} \quad c_{nq} = \frac{\partial c_n}{\partial\left(\frac{\dot{\Theta} R}{V_\infty}\right)} \quad c_{nr} = \frac{\partial c_n}{\partial\left(\frac{\dot{\Psi} R}{V_\infty}\right)}
\end{aligned} \tag{10}$$

These aerodynamic derivatives can be obtained analytically [2, 3, 6] or experimentally. Considering the symmetry, they can be expressed as follows:

$$\begin{aligned}
&c_{z\Psi} = c_{y\Theta};\ c_{m\Psi} = -c_{n\Theta};\ c_{mq} = c_{nr};\ c_{zr} = c_{yq}; \\
&c_{z\Theta} = -c_{y\Psi};\ c_{n\Psi} = c_{m\Theta};\ c_{mr} = -c_{nq};\ c_{yr} = -c_{zq}
\end{aligned} \tag{11}$$

Neglecting the low value derivatives, we can consider:

$$c_{mr} = -c_{nq} = 0; c_{yr} = -c_{zq} = 0 \tag{12}$$

By substituting Eq. (10) into the equations of motion (Eq. (6)) and considering the harmonic motion

$$[\Theta, \Psi] = \left[\overline{\Theta}, \overline{\Psi}\right] e^{j\omega t} \tag{13}$$

we obtain the final whirl flutter matrix equation

$$\left(-\omega^2[\mathrm{M}] + j\omega\left([\mathrm{D}] + [\mathrm{G}] + q_\infty F_P \frac{D_P^2}{V_\infty}\left[\mathrm{D}^A\right]\right) + \left([\mathrm{K}] + q_\infty F_P D_P\left[\mathrm{K}^A\right]\right)\right) \left| \begin{matrix} \overline{\Theta} \\ \overline{\Psi} \end{matrix} \right| = \{0\} \tag{14}$$

where the mass matrix becomes

$$[\mathrm{M}] = \begin{bmatrix} J_Y & 0 \\ 0 & J_Z \end{bmatrix} \tag{15}$$

the structural damping matrix becomes

$$[\mathrm{D}] = \begin{bmatrix} \dfrac{\mathrm{K}_\Theta \gamma_\Theta}{\omega} & 0 \\ 0 & \dfrac{\mathrm{K}_\Psi \gamma_\Psi}{\omega} \end{bmatrix} \tag{16}$$

the gyroscopic matrix becomes

$$[\mathrm{G}] = \begin{bmatrix} 0 & \mathrm{J}_\chi \Omega \\ -\mathrm{J}_\chi \Omega & 0 \end{bmatrix} \tag{17}$$

the structural stiffness matrix becomes

$$[\mathrm{K}] = \begin{bmatrix} \mathrm{K}_\Theta & 0 \\ 0 & \mathrm{K}_\Psi \end{bmatrix} \tag{18}$$

the aerodynamic damping matrix becomes

$$\left[\mathrm{D}^{\mathrm{A}}\right] = \begin{bmatrix} -\dfrac{1}{2}\mathrm{c}_{\mathrm{mq}} - \dfrac{\mathrm{a}^2}{\mathrm{D}_\mathrm{P}^2}\mathrm{c}_{\mathrm{z}\Theta} & \dfrac{1}{2}\dfrac{\mathrm{a}}{\mathrm{D}_\mathrm{P}}\mathrm{c}_{\mathrm{yq}} - \dfrac{\mathrm{a}}{\mathrm{D}_\mathrm{P}}\mathrm{c}_{\mathrm{n}\Theta} - \dfrac{\mathrm{a}^2}{\mathrm{D}_\mathrm{P}^2}\mathrm{c}_{\mathrm{y}\Theta} \\ -\dfrac{1}{2}\dfrac{\mathrm{a}}{\mathrm{D}_\mathrm{P}}\mathrm{c}_{\mathrm{yq}} + \dfrac{\mathrm{a}}{\mathrm{D}_\mathrm{P}}\mathrm{c}_{\mathrm{n}\Theta} + \dfrac{\mathrm{a}^2}{\mathrm{D}_\mathrm{P}^2}\mathrm{c}_{\mathrm{y}\Theta} & -\dfrac{1}{2}\mathrm{c}_{\mathrm{mq}} - \dfrac{\mathrm{a}^2}{\mathrm{D}_\mathrm{P}^2}\mathrm{c}_{\mathrm{z}\Theta} \end{bmatrix} \tag{19}$$

and the aerodynamic stiffness matrix becomes

$$\left[\mathrm{K}^{\mathrm{A}}\right] = \begin{bmatrix} \dfrac{\mathrm{a}}{\mathrm{D}_\mathrm{P}}\mathrm{c}_{\mathrm{z}\Theta} & \mathrm{c}_{\mathrm{n}\Theta} + \dfrac{\mathrm{a}}{\mathrm{D}_\mathrm{P}}\mathrm{c}_{\mathrm{y}\Theta} \\ -\mathrm{c}_{\mathrm{n}\Theta} - \dfrac{\mathrm{a}}{\mathrm{D}_\mathrm{P}}\mathrm{c}_{\mathrm{y}\Theta} & \dfrac{\mathrm{a}}{\mathrm{D}_\mathrm{P}}\mathrm{c}_{\mathrm{z}\Theta} \end{bmatrix} \tag{20}$$

Equation (14) can be solved as an eigenvalue problem. The critical state emerges for a specific combination of the parameters V_∞ and Ω, for which the angular velocity ω becomes real.

The influences of the main structural parameters are shown in the next figures. **Figure 6** shows the influence of the propeller advance ratio ($V_\infty/(\Omega R)$) on the stability of an undamped gyroscopic system. Increasing the propeller advance ratio has a destabilising effect. Another important parameter is the propeller hub distance ratio (a/R), the influence of which is documented in **Figure 7**. **Figure 7** also shows the influence of the structural damping (γ), which is a significant stabilisation factor. In contrast, the influence of the propeller thrust is negligible. The most critical state is $\omega_\Theta = \omega_\Psi$, when the interaction of both independent yaw and pitch motions is maximal and the trajectory of the gyroscopic motion is circular. Considering rigid propeller blades, the whirl flutter inherently appears in the backward gyroscopic mode. The flutter frequency is the same as the frequency of the backward gyroscopic mode. The critical state can be reached by increasing either V_∞ or Ω. A special case of eq. (14) for $\omega = 0$ is gyroscopic static divergence, which is characterised by unidirectional divergent motion.

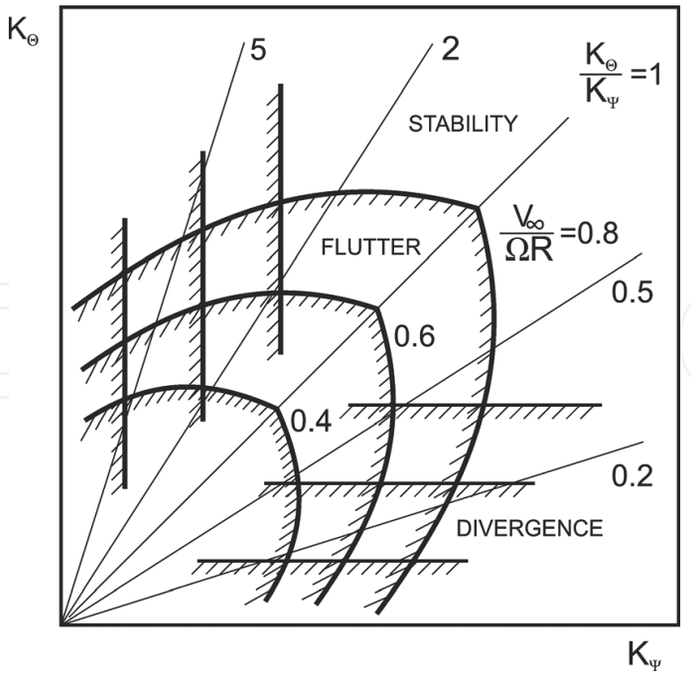

Figure 6. Influence of the propeller advance ratio on the stability of an undamped gyroscopic system.

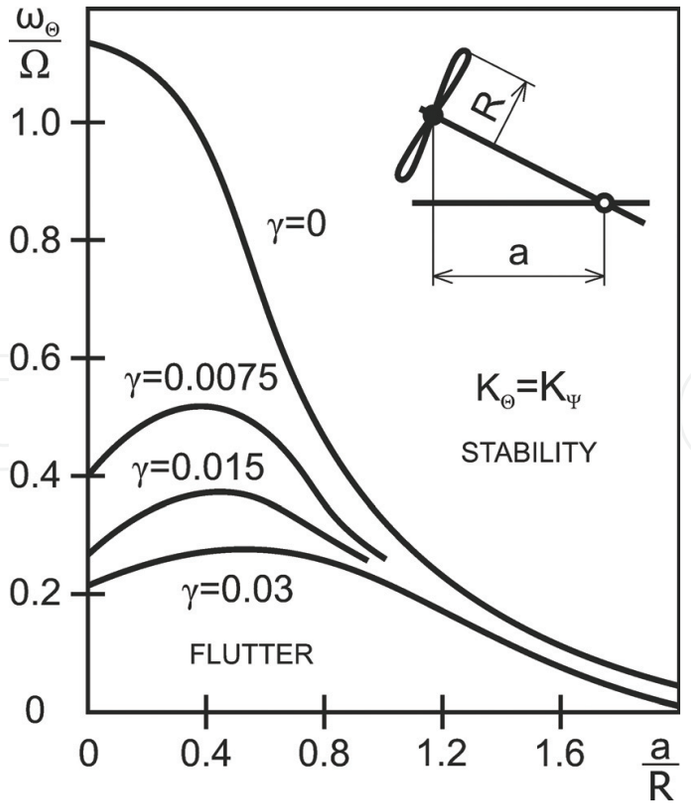

Figure 7. Influence of the propeller hub distance ratio.

http://dx.doi.org/10.5772/intechopen.70171

The described model, which is based on the assumption of a rigid propeller, is obviously applicable for standard turboprop aircraft (commuters, utility aircraft, and military trainers), for which the natural frequencies of the propeller blades are much higher than the frequencies of the engine system suspension vibrations. In large turboprops, in particular military transport aircraft with heavy multiblade propellers, the solution requires taking into account the deformations of the propeller blades as well [7–10]. Obviously, whirl flutter investigation of tilt-rotor aircraft must include even more complex analytical models [11, 12].

3. Experimental research

The analytically obtained results on the complicated physical principles of whirl flutter require experimental validation of the analytically obtained results, especially due to the unreliable analytical solution of the propeller aerodynamic forces. In addition, structural damping is a key parameter, to which whirl flutter is extremely sensitive and the characteristics of which need to be validated. Therefore, experiments using aeroelastic models are required.

Most of the developments in the whirl flutter experimental research were accomplished in the early 1960s. The experiments were carried out in direct connection with the Electras' accidents. The first experimental investigations were accomplished by Houbolt and Reed [6]. They used the simple model of a propeller in the windmilling mode. The complex investigations of whirl flutter characteristics were conducted by Bland and Bennett [13]. The measurements, which were carried out in the NASA Langley wind tunnel were focused on the propeller forces and stability of the propeller-nacelle component model. As was typical, a propeller rotated in the windmilling mode. The experimental results showed that the theoretical aerodynamic derivatives underestimated the whirl flutter speed and the application of the experimentally obtained derivatives to the analytical solution made the solution much closer to the experimental results. The tilt-rotor concept was researched by Reed and Bennett [14], who focused on the flight regimes of high inflow angles. Apart from the rigid blades, they also accounted for blades' flexibility when conducting the experiment on a simple model with flapping blades. Both backward and forward whirl mode instabilities occurred during the tests of the flapping-blade model. Similar experiments on the flapped blade rotor system were accomplished by Krishna Rao and Sundararajan [7] in NAL Bangalore. The influence of the blades' flapping frequency on the whirl flutter stability for both backward and forward whirl modes was demonstrated by these experiments.

A more complex model, which represented an aircraft half-wing with an engine, was tested by Bland and Bennett [15] in NASA Langley. That model was a typical aeroelastic model with a duralumin spar and balsa segment structure. The main focus of these experiments was to investigate the influence of wing stiffness on whirl flutter.

The largest experimental campaign was accomplished as a part of the response to the L-188 C Electra II aircraft accidents. Eventually, the tests helped to determine the cause of the accidents: whirl flutter. The aeroelastic model included four nacelles and four windmilling propellers. The model represented a full-span aircraft due to the investigation of the unsymmetrical

phenomena. The model was flown in a wind tunnel with sufficient lift during the measurements and the trimmed flight was maintained by an operator controlling the horizontal stabilizer. Various configurations with reduced starboard outboard engine attachment stiffness were tested with the aim of identifying the causes of the aircraft accidents. The reduced stiffness parameters were also tested on the inboard power plant, and the combination of two engines was also tested. States with reduced damping were also tested. The experiments are summarised by Abbott et al. [16].

Further experimental activities were primarily focused on the issues connected with the design and development of tilt-rotor aircraft, such as the Bell XV-3 or XV-15, Bell-Boeing V-22 Osprey, Agusta-Westland AW609, and XC-142A. A large investigation of the proprotor research model with flapping blades was conducted by Kvaternik and Kohn [17]. The stiffness of the nacelle attachment was reduced to reach the flutter boundaries within low velocities. The main aim of the work was the necessity to establish an experimental database for proprotor whirl flutter prediction with sufficient confidence. A total of 26 backward whirl flutter states and 50 forward whirl flutter states were found.

Recent experimental studies include the work performed by Rand and Peyran [18]. The tests were aimed at assessing the effects of the noted structural characteristics couplings on the whirl flutter of the proprotor during forward flight. In addition, the possibility of suppressing the instability by means of the active control of the wing's structural characteristics was tested. The demonstrator included a proprotor in windmilling mode attached to the wing structure. A very simple table-top model was used by Acree et al. [19]. The model included weights in front of the leading edge of the blades' tips. Moving the weights chordwise caused significant changes in the whirl mode stability.

A large model of the tilt-rotor aircraft concept, including a half-wing and proprotor, was tested for whirl flutter in the DNW wind tunnel in the Netherlands. The model was based on an aerodynamic wind tunnel model of a previous project. Therefore, aeroelastic scaling and modifications were limited. A multibody analysis based on available technical information was reported by Krueger [20].

Experimental activities that employed a model of a tilt-rotor aircraft component or a complete tilt-rotor aircraft model were performed on the WRATS aeroelastic demonstrator. The complete model was based on the 1/5-size semispan aeroelastic model of the V-22 Osprey aircraft. The model was used during the development of the Osprey to improve the stability characteristics of the aircraft. Later, the model was modified and utilized as the research demonstrator for active control research. WRATS-related activities are summarised by Piatak and Kvaternik et al. [21] and by Nixon et al. [22].

The latest experimental activities were accomplished by Cecrdle et al. using the W-WING aeroelastic demonstrator [23]. The demonstrator was adapted from a half-wing with a span of 2.56 m with the engine of a former aeroelastic model of a commuter aircraft for 40 passengers. The total mass of the model is approximately 55.5 kg. The stiffness of the wing and aileron is modeled by a duralumin spar of variable cross-section. The aerodynamic shape is covered with modular balsa and plastic segments. The inertia characteristics are modeled by lead weights.

The aileron actuation stiffness is modeled by means of a replaceable steel spiral spring. Optionally, the aileron may be actuated by the hydraulic actuator or by the electromagnetic shaker placed at the wing root via a push-pull rod. Furthermore, an active control system that is capable of simulating the additional mass, damping, or stiffness, including the nonlinear characteristics of these terms [24], may also be applied. The wing is fixed at the root to the pylon that is attached to the wind tunnel manipulator.

The nacelle structure may be used either separately or attached to the wing structure as described. The influence of changes in the main parameters on the whirl flutter may be simulated by the demonstrator. The nacelle model includes two degrees of freedom (engine yaw and pitch). The engine attachment stiffness parameters are modeled using cross spring pivots. The leaf springs are changeable. The stiffness parameters can be adjusted independently by replacing the spring leaves. Both pivots are independently movable in the direction of the propeller axis. This allows for the adjustment of the pivot points of both vibration modes, while the overall length of the nacelle and the propeller position remain the same. The engine inertia parameters are modeled by a replaceable and movable weight. The weight is used to preserve position of the center of gravity in case the pivot stations change. Optionally, it also enables the position of the center of gravity to be changed. Provided the nacelle is attached to the wing, the wing dynamic characteristics can also be adjusted to evaluate the influence of the wing structure on the whirl flutter. The design solution of the engine attachment is shown in **Figure 8**.

Sensor instrumentation of the wing includes strain gauges in the root and half-span sections that are configured to measure the torsional, vertical bending, and in-plane bending deformations. In addition, the demonstrator is equipped with accelerometers at the front of the engine and at the wing-tip section. Accelerometers measure the vertical and lateral acceleration.

Figure 8. Design solution of W-WING demonstrator engine attachment, motor, and propeller.

The gyroscopic effect is simulated by the rotating mass of the propeller blades. Actually, two sets of blades are available (light, made of duralumin, and heavy, made of steel). The propeller of 0.7 m diameter represents a scaled-down real 5-blade propeller. The propeller is powered by an electric motor and it can operate at arbitrary revolutions of up to 3000 rpm. Obviously, the windmilling mode is also applicable. The propeller blades are adjustable at a standstill. There are several blade adjustment options (angles of attack) that are applicable for specific ranges of the flow velocity. Additionally, the blade angle of attack may be used to manage the revolutions of the windmilling propeller.

The tests were performed in the VZLU 3-m-diameter low-speed wind tunnel. To prevent the induced effects at the wing root region, the wing is combined with the splitter plate. The demonstrator is fixed to the attachment arm inside the wind tunnel test section. Both the angle of attack and angle of sideslip of the tested model may be changed, provided if requested. The test arrangement is shown in **Figure 9**.

The measurement variants of the model were defined by the following structural parameters: pitch and yaw attachment stiffness, pitch and yaw hinge station, mass-balance weight station, choice of propeller (duralumin or steel blades), and finally, the propeller blade's 75%-section angle of attack (α).

The tests were focused on the variation of the pitch and yaw stiffness first. During these tests, the most promising variants with respect to the pitch and yaw stiffness, which showed the largest vibrations, were found and used as the baselines during the next phase of the tests. Then, the variations of the blade angle of attack, choice of a light or heavy propeller, and variation of the pitch hinge station and mass-balance weight station were examined. The measurements included excitation by the flow turbulence and by the aileron flapping sweep. The latter was found as very useful for the estimation of whirl mode damping.

The next figures show examples of the experimental results. The figures show evaluated whirl mode parameters as functions of the windflow speed. These parameters are propeller revolutions,

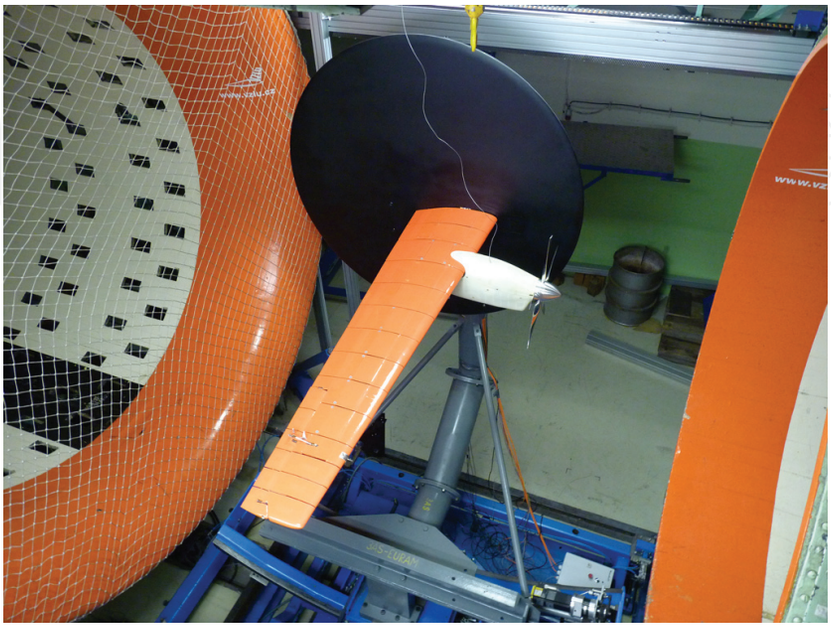

Figure 9. W-WING demonstrator in the wind tunnel test section.

damping, and frequency of the whirl mode and the maximal amplitude (pitch or yaw) of the front engine sensor section. The first example (**Figure 10**) demonstrates a very stable case. The vibration amplitude of the structure is very low and the damping increases with the windflow velocity.

The next example (**Figure 11**) shows the case in which the instability was reached. The amplitude curve shows a rapid increase near the flutter velocity. Additionally, the damping reaches

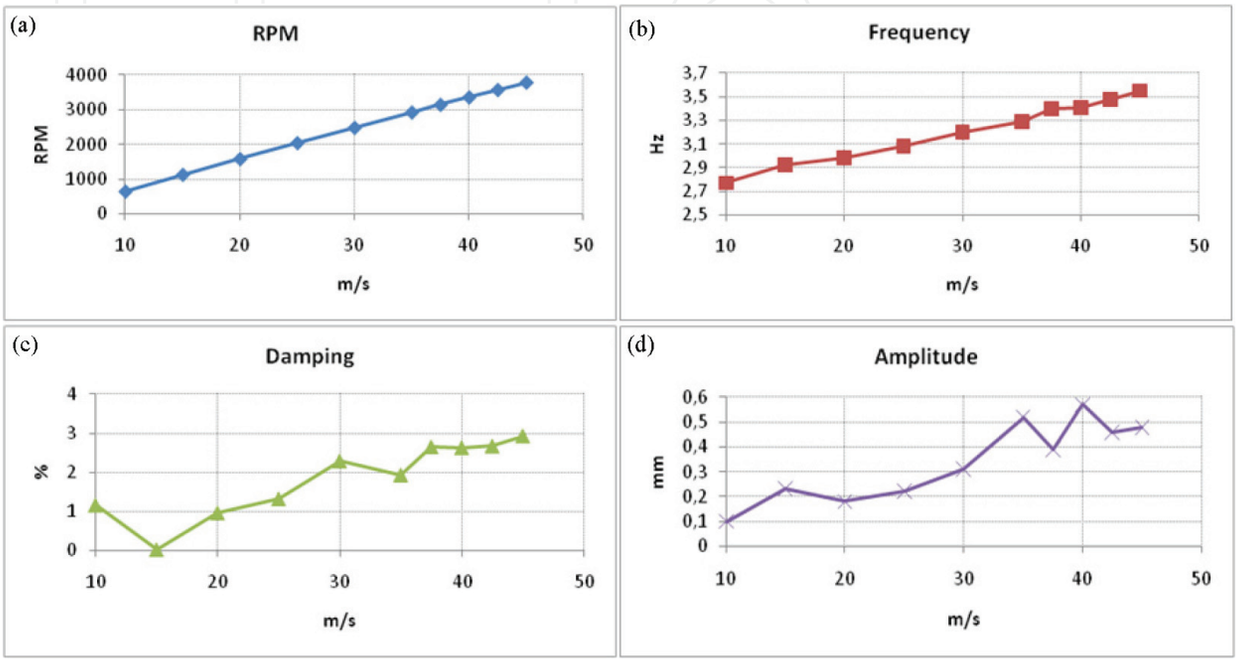

Figure 10. Whirl mode parameters: (a) propeller rpm, (b) whirl mode frequency, (c) whirl mode damping, (d) yaw or pitch amplitude. Stable case (pitch spring: nr.2, yaw spring: nr.2, pitch hinge: middle, weight: rear, blades: heavy, $\alpha = 2.5°$).

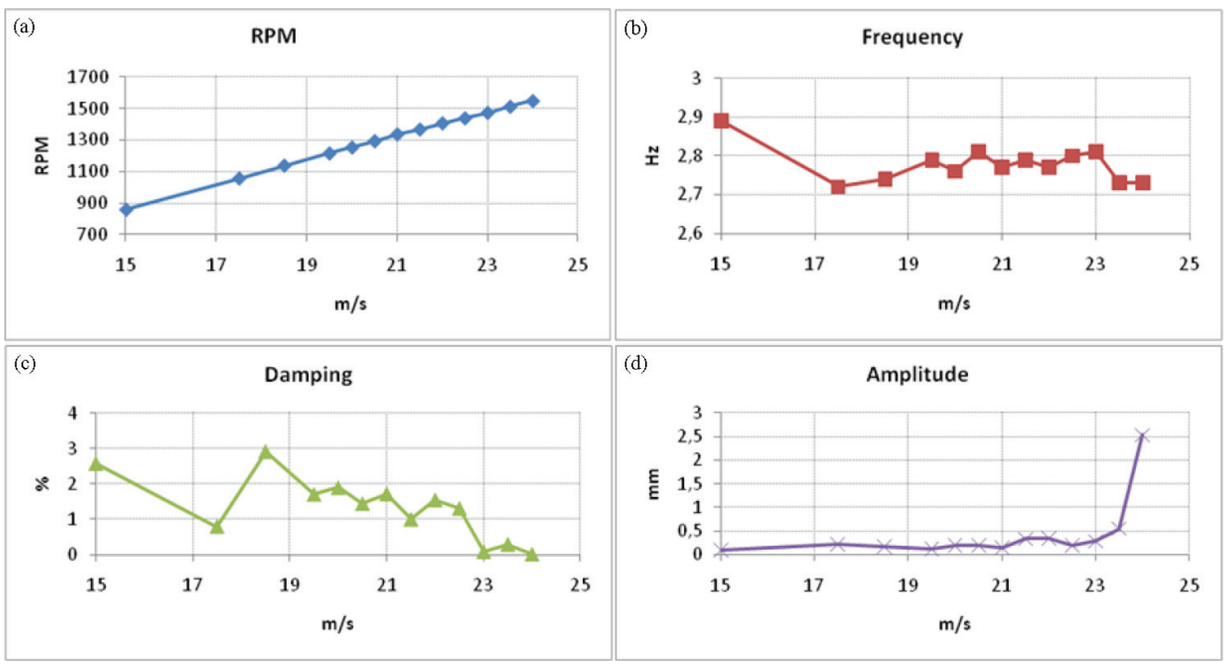

Figure 11. Whirl mode parameters: (a) propeller rpm, (b) whirl mode frequency, (c) whirl mode damping, (d) yaw or pitch amplitude. Unstable case (pitch spring: nr.2, yaw spring: nr.2, pitch hinge: middle, weight: front, blades: light, $\alpha = 0°$).

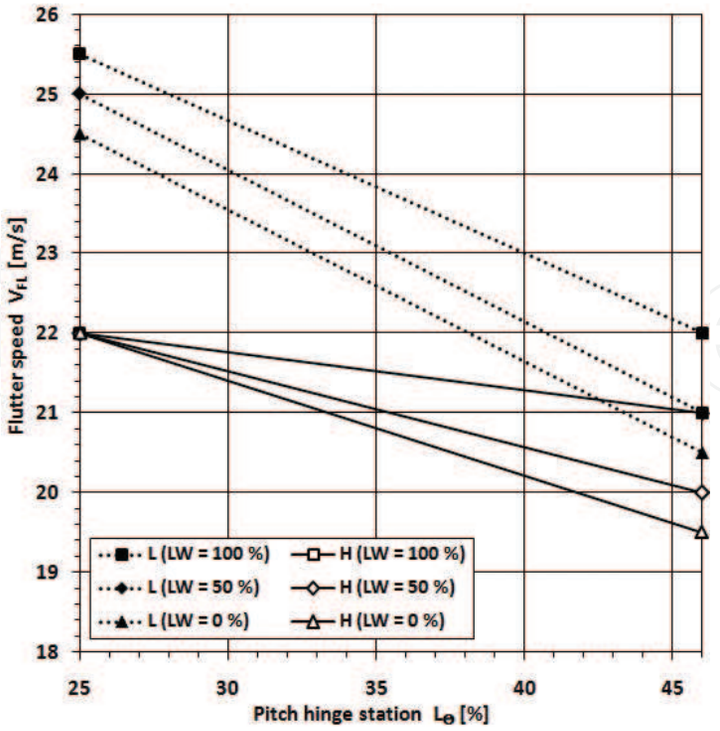

Figure 12. Influence of pitch hinge station (L_Θ) on flutter speed (25% = rear; 46% = middle; L = light blades; H = heavy blades; LW = mass-balance weight station).

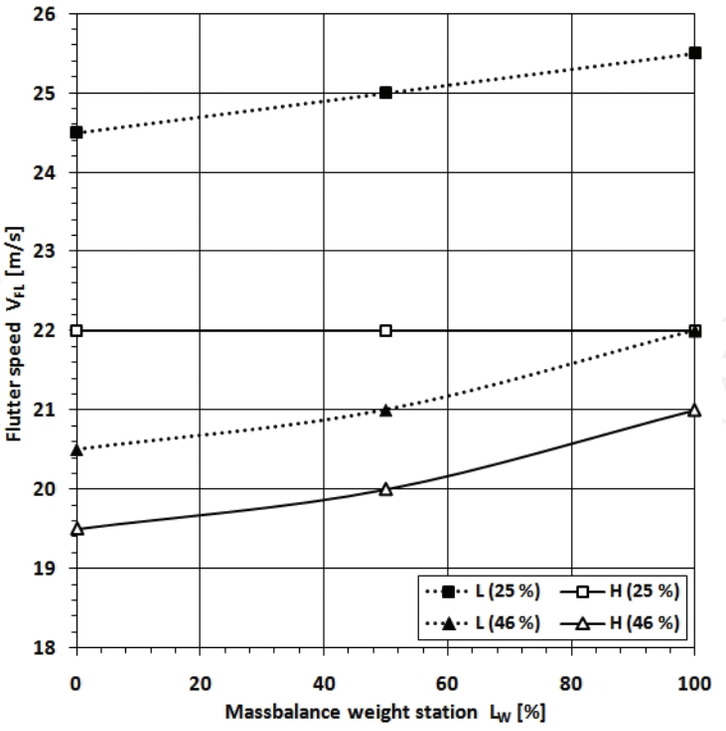

Figure 13. Influence of mass balance weight station (L_W) on flutter speed (0% = front; 100% = rear; L = light blades; H = heavy blades), rear (25%), and middle (46%) pitch hinge stations.

zero. The damping curve represents the damping values given by operational modal analysis (OMA). These damping values, which were obtained by the evaluation of the logarithmic decrement, are very small negative values, which are not noticeable in the figure. A negative damping value represents an unstable state. The unstable states with higher negative damping could not be reached due to safety reasons.

Figures 12 and **13** show more detailed information regarding the influence of the parameters. The influence of the pitch hinge station is demonstrated in **Figure 12**. Moving the hinge rearward increases the a/R ratio, and therefore, has a positive effect on flutter stability. The influence of the mass-balance weight station is demonstrated in **Figure 13**. Moving the weight rearward causes a decrease in mass moments of inertia (J_Y and J_Z) and the related increase in the yaw and pitch frequency (f_Ψ and f_Θ), and therefore, it also has a positive effect on flutter stability. Flutter speeds of configurations with heavy blades are lower compared to the flutter speeds with light blades as the heavy blades reduce both the yaw and pitch frequencies (f_Ψ and f_Θ).

4. Certification process

The airworthiness regulation standard requirements for dealing with the aeroelasticity and flutter also include requirements related to the whirl flutter. Essentially, the whirl flutter requirements are applicable only to aircraft powered by a turboprop power plant system. In the following text, the requirements of the FAR/CS 23 regulation standard, which is applicable to smaller turboprop aircraft, are taken into consideration. The whirl flutter related requirement, which is included in §629(e), is applicable regardless of the aircraft configuration or the number of engines (twin wing-mounted, single nose-mounted, twin fuselage mounted pusher, etc.). §629(e)(1) includes the main requirement to evidence the stability within the required V-H envelope, while §629(e)(2) requires the variation of structural parameters such as the stiffness and damping of the power plant attachment. The whirl flutter analysis must, therefore, include all significant aircraft configurations with respect to fuel and payload that are applicable to the aircraft operation. The whirl flutter analysis must also include the influence of the variance of the power plant mount structural parameters when simulating the possible changes due to structural damage (e.g., deterioration of engine mount isolators). Note that further requirements that are applicable to aircraft compliance with the fail-safe criteria come from §629(g).

We can use two main approaches for the analysis:

First is the standard approach, in which the analyses are performed for a known set of structural parameters, and the results are whirl flutter stability characteristics (e.g., whirl flutter speed). The resulting flutter speed is then compared to the certification velocity according to the flight envelope. The analyses are performed sequentially, state by state.

The standard approach is good for complying with the main requirement (§629(e)(1)), which is realized by evaluation of the nominal parameter states. **Figure 14** shows an example of a V-g-f diagram of such a calculation. No flutter instability is indicated up to the certification velocity, which is 191.4 m/s in the case, and therefore, the regulation requirement is fulfilled. Calculations are performed for all applicable mass configurations. However, for parametric studies that

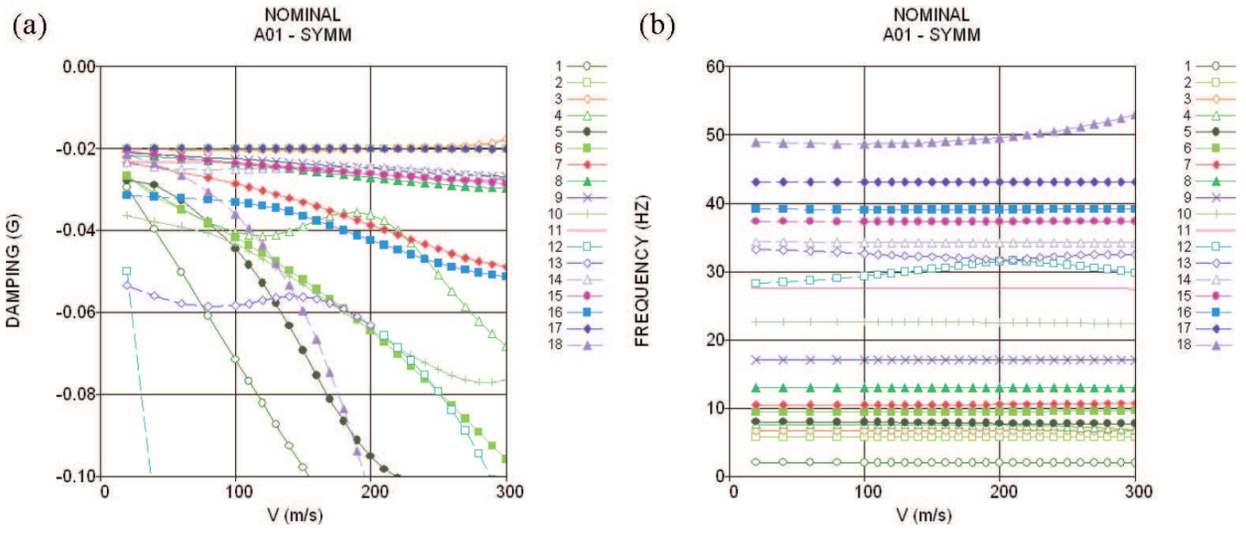

Figure 14. Example of whirl flutter calculation (V-g-f) diagram, (a) damping, (b) frequency, nominal state.

may include huge numbers of analyses, such an approach may become ineffective unless some tool for automated analysis, data handling, and processing is used. However, the applicability of such automatic processing systems is always limited.

Therefore, to comply with the parameter variation requirement (§629(e)(2)), the second, optimization-based approach [25] can be used. In this approach, the flutter speed is set equal to the certification speed, and the results are critical values of the structural parameters. The stability margin can then be obtained from these critical structural parameters. The analyzed states are then compared only with respect to the structural parameters and the relationship to the stability margin. Such an approach can save large amounts of time because the number of required whirl flutter analyses is dramatically reduced.

Provided a full-span model is considered, four design variables are defined: (1) effective stiffness of the engine attachment for symmetric pitch, (2) effective stiffness of the engine attachment for antisymmetric pitch, (3) effective stiffness of the engine attachment for symmetric yaw, and (4) effective stiffness of the engine attachment for antisymmetric yaw. The solution includes three frequency ratio constraints: (1) for symmetric engine vibration frequencies, (2) for antisymmetric engine vibration frequencies, and (3) for critical whirl flutter frequencies. Additionally, the flutter constraint, i.e., the requirement of flutter stability, is applied for the certification speed. The objective function is then formally expressed as the minimization of the sum of engine vibration frequencies. **Figure 15** shows an example of a V-g-f diagram for the optimization-based calculation. There is a flutter state of mode nr.2 (engine pitch vibration mode) at the velocity of 191.4 m/s representing the whirl flutter instability. Calculations are performed for several values of the critical frequency ratio to construct a stability margin curve, which is then constructed for all applicable mass configurations, as shown in the example in **Figure 16**. Stability margins may be constructed with respect to either engine yaw and pitch vibration frequency or engine yaw and pitch attachment effective stiffness. The former type of margin is then compared with the engine vibration frequencies, obtained by the GVT or analytically, to evaluate the rate of reserve. **Figure 17** demonstrates an example of such an evaluation. The

http://dx.doi.org/10.5772/intechopen.70171

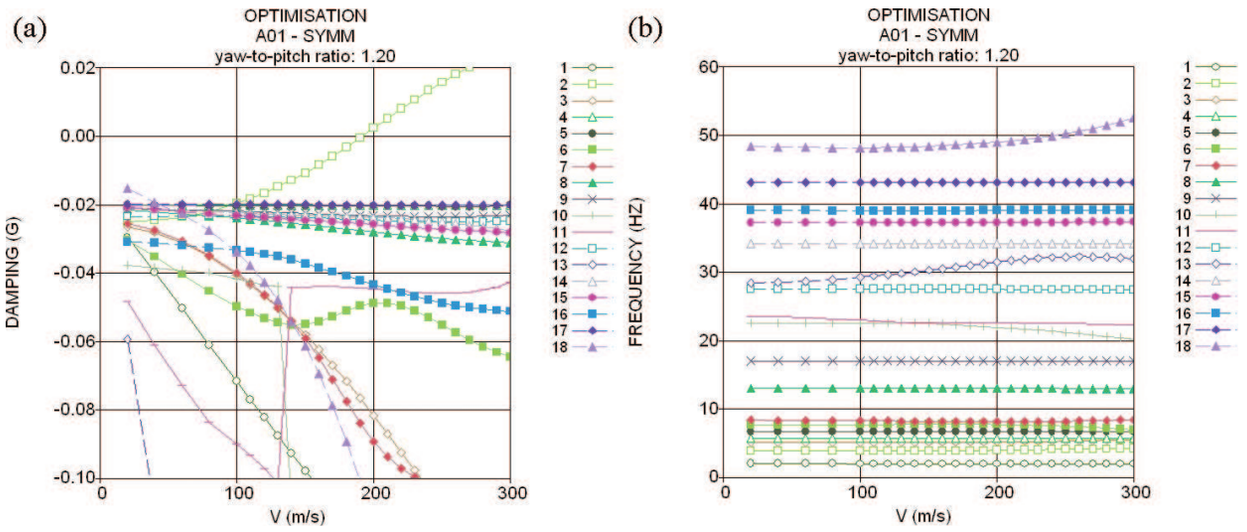

Figure 15. Example of whirl flutter calculation (V-g-f) diagram, (a) damping, (b) frequency, optimization-based calculation.

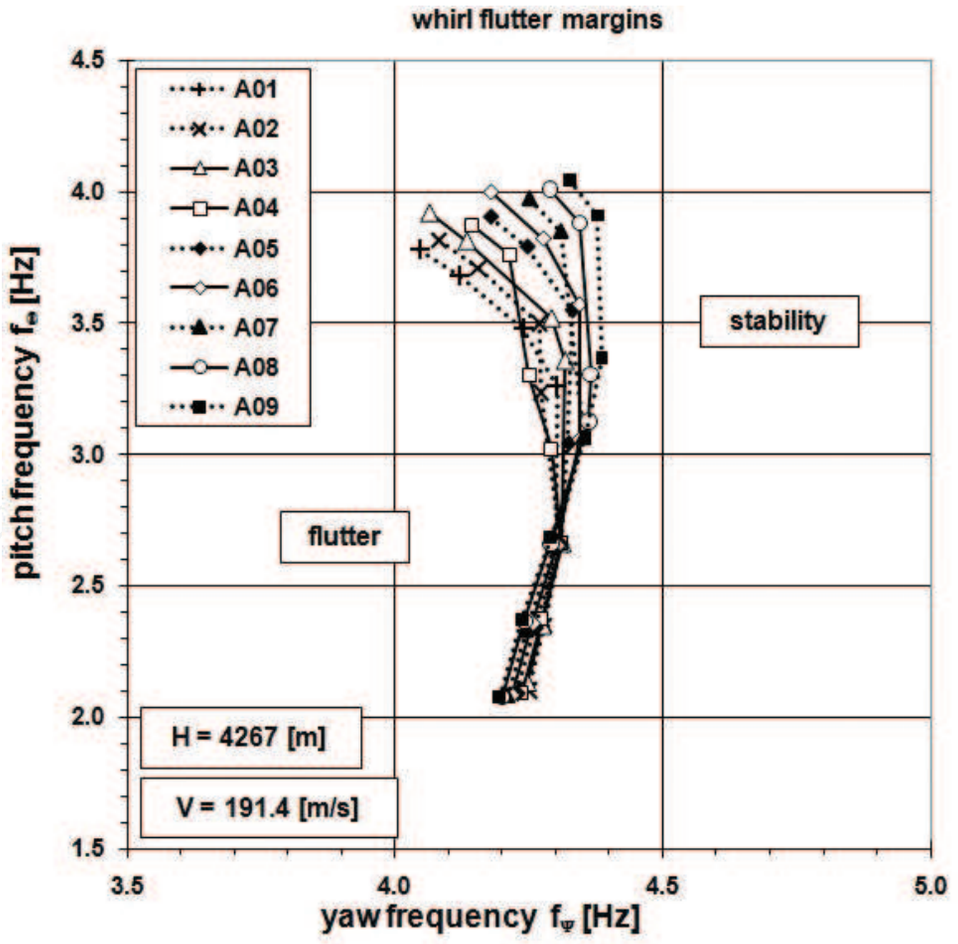

Figure 16. Example of whirl flutter stability margins for multiple mass configurations.

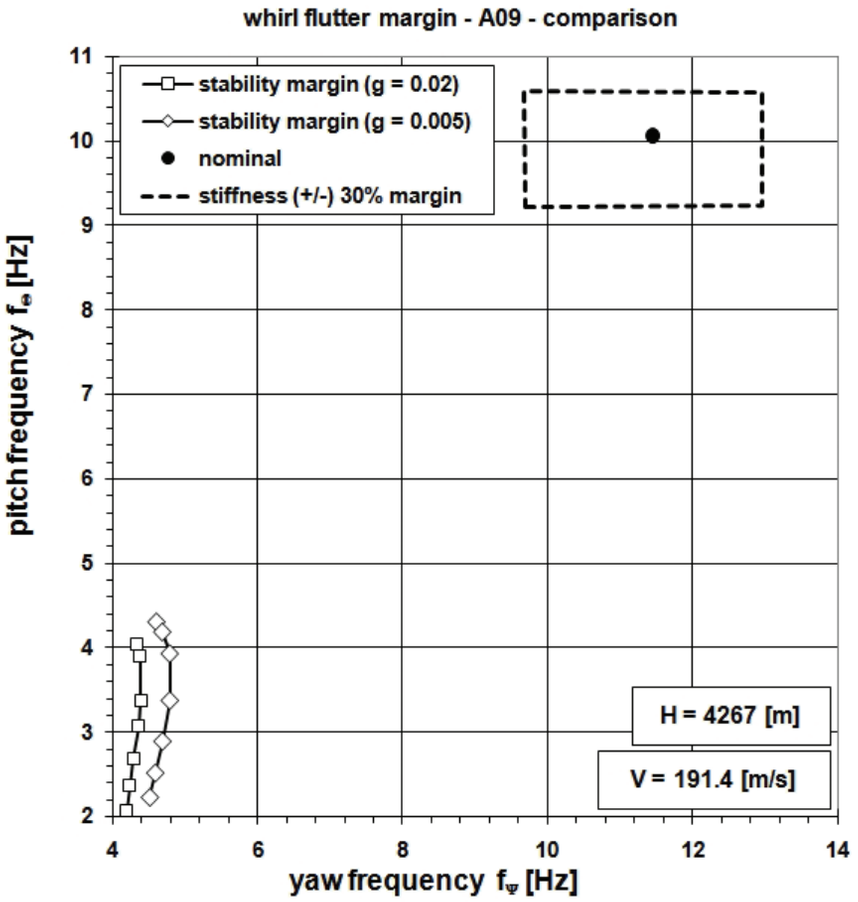

Figure 17. Example of whirl flutter stability margin evaluation.

dashed line represents the (±) 30% variance margin in engine attachment stiffness. Another parameter to be evaluated is the damping. This is provided by calculation with very low structural damping, represented by the damping of $g = 0.005$, while the standard structural damping included in the analyses is $g = 0.02$. The stability margin for reduced damping is also presented in **Figure 17**.

As obvious from **Figure 17**, there is sufficient reserve in stability of the nominal state with respect to the stability margin, and therefore, the regulation requirements would are fulfilled.

5. Conclusion

The presented chapter addresses a specific aeroelastic phenomenon that is applicable for turboprop aircraft structures: whirl flutter. This chapter includes basic facts regarding the physical principles and the analytical solution of the described phenomenon. After that, the experimental research activities are outlined, with a focus on the recent experiments on the W-WING whirl flutter demonstrator. Finally, the approaches to aircraft certification are explained. Comprehensive information on the whirl flutter phenomenon from all aspects can be found in Ref. [26].

Acknowledgements

This work was supported by the institutional support of nonprofit research organisations by the Ministry of Industry and Trade of the Czech Republic.

Author details

Jiří Čečrdle

Address all correspondence to: cecrdle@vzlu.cz

Aeronautical Research and Test Institute (VZLU), Prague, Czech Republic

References

[1] Taylor ES, Browne KA. Vibration isolation of aircraft power plants. Journal of Aerospace Sciences. 1938;**6**:43-49

[2] Ribner HS. Propellers in Yaw. Langley: NASA Report 820; 1945

[3] Ribner HS. Formulas for Propellers in Yaw and Charts of the Side-Force Derivatives. Langley: NASA Report 819; 1945

[4] Donham RE, Watts GA. Whirl flutter first case. In: Flomenhoft H, editor. The Revolution in Structural Dynamics. 1st ed. Palm Beach Gardens: Dynaflo Press; 1997. pp. 99-109

[5] Reed WH. Review of Propeller-Rotor Whirl Flutter. Langley: NASA Report TR R-264; 1967

[6] Houbolt JC, Reed WH. Propeller-Nacelle whirl flutter. Journal of Aerospace Sciences. 1962;**3**:333-346

[7] Krishna Rao KV, Sundararajan D. Whirl Flutter of Flapping Blade Rotor Systems. Bangalore: National Aeronautical Laboratory TN-18; 1969

[8] Richardson JR, Naylor HFW. Whirl Flutter of Propellers With Hinged Blades. Toronto: Engineering Research Associates Report No. 24; 1962

[9] Richardson JR, McKillop JA, Naylor HFW, Bandler PA. Whirl Flutter of Propellers with Flexible Twisted Blades. Toronto: Engineering Research Associates Report No. 43; 1962

[10] Donham RE. Effect of propeller blade bending dynamics on 1P loads and whirl flutter. In: International Forum on Aeroelasticity and Structural Dynamics; 28 June-1 July 2005; Munich

[11] Barkai SM, Rand O, Peyran RJ, Carlson RM. Modeling and analysis of tilt-rotor aeromechanical phenomena. Mathematical and Computer Modelling. 1998;**12**:17-43

[12] Dugeai A, Mauffrey Y, Sicot F. Aeroelastic capabilities of the elsA solver for rotating machines applications. In: International Forum on Aeroelasticity and Structural Dynamics; 26-30 June 2011; Paris

[13] Bland SR, Bennett RM. Wind-Tunnel Measurement of Propeller Whirl-Flutter Speeds and Static Stability Derivatives and Comparison with Theory. Langley: NASA Report TN D-1807; 1963

[14] Reed WH, Bennett RM. Propeller Whirl Flutter Considerations for V/STOL Aircraft. In: CAL/TRECOM Symposium; Buffalo; 1963

[15] Bennett RM, Bland SR. Experimental and Analytical Investigation of Propeller Whirl Flutter of a Power Plant on a Flexible Wing. Langley: NASA Report TN D-2399; 1964

[16] Abbott FT, Kelly HN, Hampton KD. Investigation of Propeller Power Plant Autoprecession Boundaries for a Dynamic-Aeroelastic Model of a Four-Engine Turboprop Transport Airplane. Langley: NASA Report TN D-1806; 1963

[17] Kvaternik RG, Kohn JS. An Experimental and Analytical Investigation of Proprotor Whirl Flutter. Langley: NASA Report TP 1047; 1977

[18] Rand O, Peyran RJ. Experimental demonstration of the influence of wing couplings on whirl–flutter instability. Journal of Aircraft. 2000;**5**:859-864

[19] Acree CW, Peyran RJ, Johnson W. Rotor design for whirl flutter: An examination of options for improving tiltrotor aeroelastic stability margins. In: American Helicopter Society 55th Annual Forum; 25-27 May 1999; Montreal

[20] Krueger WR. Analysis of whirl flutter dynamics on a tiltrotor wind tunnel model. In: International Forum of Aeroelasticity and Structural Dynamics; 21-25 June 2009; Seattle

[21] Piatak DJ, Kvaternik RG, Nixon MW, Langston ChW, Singleton JD, Bennett RL, Brown RK. A wind-tunnel parametric investigation of tiltrotor whirl-flutter stability boundaries. In: American Helicopter Society 57th Annual Forum; 9-11 May 2001; Washington

[22] Nixon MW, Langston ChW, Singleton JD, Piatak DJ, Kvaternik RG, Corso LM, Brown RK. Aeroelastic stability of a four-bladed semi articulated soft inplane tiltrotor model. In: American Helicopter Society 59th Forum; 6-8 May 2003; Phoenix

[23] Cecrdle J, Malinek P, Vich O. Wind tunnel test of whirl flutter aeroelastic demonstrator. In: 58th AIAA/ASCE/AHS/ASC Structures, Structural Dynamics, and Materials Conference; 9-13 January 2017; Grapevine. DOI: 10.2514/6.2017-0635

[24] Malecek J, Cecrdle J, Hlavaty V, Malinek P. Mechanical concepts for simulation of nonlinearities on aeroelastic demonstrator. Journal of Aircraft. 2013;**2**:651-658

[25] Cecrdle J. Analysis of twin turboprop aircraft whirl-flutter stability boundaries. Journal of Aircraft. 2012;**6**:1718-1725. DOI: 10.2514/1.C031390

[26] Cecrdle J. Whirl Flutter of Turboprop Aircraft Structures. 1st ed. Oxford: Elsevier Science; 2015. p. 354